Investigation of Structural and Microbial Properties of Samarium-Doped Nickel-Strontium Ferrite Nanoparticles Prepared via the Sol-Gel Route

Published: 19 June 2023

Volume 13, pages 1126–1139, (2023) Cite this article

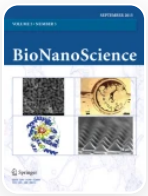

BioNanoScience

Aims and scope

Submit manuscript

Rajkanya M. Bhore, Radhakrishnan M. Tigote, Subiya K. Kazi, Sanjay R. Chavan, Rahul M. Khobragade & Girdharilal B. Tiwari

Abstract

Nickel and samarium-doped strontium ferrite nanoparticles were synthesized using the sol-gel auto-combustion method. The micro-structural characteristics of the ferrite were investigated using X-ray diffraction (XRD) and field-emission scanning electron microscopy (FE-SEM). It was determined that the particle size ranged from 30 to 60 nm, which was confirmed by TEM as well. The vibrating sample magnetometer (VSM)

revealed a strong magnetization with paramagnetic behaviour, and the existence of all elements was verified by energy dispersive X-ray spectroscopy (EDS). According to the BET adsorption isotherm, total surface area ranges from 13.77 to 28.49 $m^2 g^{-1}$. At P/Po (0.99), the total pore volume ranges from 0.02 to 0.04 $cm^3 g^{-1}$. The average pore width ranged from 3.5 to 6.5 nm, and the isotherm demonstrates type III with an H_3 hysteresis loop. The material shows 84% thermal stability and these synthesized nanoparticles are showing activity against both Gram-positive and Gram-negative bacterial pathogens. These synthesized nanoparticles are showing activity against both Gram-positive, Gram-negative bacteria and fungal pathogens, indicating broad-spectrum activity against microbial pathogens. The increased concentration of compound (0.1) showed antimicrobial activity against all the pathogens, which was measured as the zone of growth inhibition in diameter (mm) and compared with the standard antibiotics, streptomycin and clotrimazole.

1 Introduction

Recent studies of matter at dimensions ranging from 1 to 100 nanometers, where unique phenomena provide innovative applications towards the physical and chemical

characteristics, In nanomaterial's, previous efforts focused on various techniques for synthesizing nanoparticles with controllable size and shape, allowing them to be tailored in terms of their characteristics [1,2,3]. Many researchers have been drawn to spinel ferrite over the last few decades due to their cubic crystalline structure, greater magnetization, and opto-electric capabilities [4]. The synthesis of nanoparticles reveals high resistivity and reduced eddy current losses; nano-sized ferrites have superior catalytic, electric, and magnetic characteristics. These materials characteristics are extremely sensitive to preparation conditions such as sintering temperature, time, and additive type [5,6,7,8,9]. The addition of a modest number of larger ions, such as rare earth, can result in significant changes in both structural and magnetic characteristics due to the fact that rare-earth ions play a significant role in determining magneto-crystalline anisotropy in 4f–3d intermetallic compounds. Rare earth ions are known to have unpaired 4f electrons, which have the function of causing magnetic anisotropy due to their orbital structure. The impact of several rare earth metal substitutions on ferrites was diverse [10, 11].Rare earth oxides are emerging as interesting additions for improving ferrite characteristics [12, 13]. The electromagnetic features of the nano-spinel structure may be easily adjusted by replacing different cations. Because of its very broad applicability, the doping of rare earth ion-replaced spinel ferrite nanoparticles has achieved a substantial increase in prominence and a remarkable change in the structural, magnetic, and electrical characteristics of ferrite due to rare earth ion substitution, some of which are on La, Gd, Eu, Dy, Er, Tb, Ce, and Y[14,15,16].

The development of appropriate coating is required to maintain the stability of magnetic iron oxide nanoparticles [17,18,19,20]. The essential characteristics of strontium ferrite were improved by doping it with several ions of varying valences. On the one hand, substituting unfamiliar ions for Fe^{3+} ions may alter the magnetic characteristics and phases that are most likely produced [21,22,23,24]. Ferrites have also been included in inductors, choke coils, recording heads, and magnetic amplifiers. These properties, together with its high chemical stability and mechanical hardness, make it suitable for electronic industries such as magnetic spin filters, data storage, microwave absorbers, and biomedical areas, where they are very useful for magnetic resonance imaging (MRI), bio-magnetic separation, tumour treatment by hyperthermia, drug delivery and release, catalysis and drug targeting [25,26,27,28,29,30,31]. The production of SmO_2 by Sm^{3+} doping lowered the relative density of ferrites. During sintering, this SmO_2 often stimulates grain expansion by replacing rare-earth ions for Fe in ferrite, causing lattice strain and structural disorder and allowing the dielectric and electrical characteristics to

be modified. These characteristics can be improved based on the distribution of cations between A- and B-sites, which is significantly influenced by the nature of the ions for their properties [32, 33]. The synthesized methods involve high-temperature calcinations using various techniques to achieve microstructure, crystallography, magnetic, optical, and dielectrical properties, including sol-gel auto-combustion, micro-emulsion method, mechanical and ball-milling, hydrothermal synthesis and co-precipitation, thermal decomposition, citrate-nitrate-assisted, electrospinning, reverse micelle, and ultra-sonication [34, 35].

We focused on the new synthesis of $Ni_{0.8-x}Sm_xSr_{0.2}Fe_2O_4$ (x = 0.02, 0.04, 0.06, 0.08, 0.1) using the sol-gel auto combustion technique, and corresponding studies of various properties such as micro-structural, band energy, size, surface area, magnetic and dielectric constants, dielectric loss, and microbial activities were used to evaluate the resulted synthesis [36,37,38,39,40,41,42,43,44,45,46,47,48,49].

Nanoparticles are playing crucial role in the treatment of various diseases. NPs can attack on the cell membrane of bacterial cells and cause damage, disorganization of cell membrane and death of cell [48]. $Ni_{0.8-x}Sm_xSr_{0.2}Fe_2O_4$ nanoparticles were subjected for antimicrobial activity against different microbial pathogens which includes bacterial and fungal pathogens. Gram-positive *Bacillus subtilis* (ATCC 6633) *Staphylococcus aureus* (ATCC6538), and Gram-negative bacteria *Escherichia coli* (ATCC 8739), and fungal species *Aspergillus niger* ATCC 16404, and *Candida albicans* ATCC 10231 were used for study.

2 Material and Methods

2.1 Materials

The required materials for the preparation of $Ni_{0.8-x}Sm_xSr_{0.2}Fe_2O_4$ are purchased from HI media and used without purification. Nickel nitrate Ni $(NO_3)_2{\cdot}6H_2O$, strontium nitrate $Sr(NO_3)_2$, samarium nitrate Sm $(NO_3)_3{\cdot}6H_2O$, and ferric nitrate Fe $(NO_3)_3{\cdot}9H_2O$ were used as sources of La, A1, Y and Fe, with citric acid as a complexing agent and to maintain neutral condition ammonia is used. All of the chemicals are of A.R. quality

2.2 Synthesis of $Ni_{0.8-x}Sm_xSr_{0.2}Fe_2O_4$ Nanomaterial

For the new synthesis of $Ni_{0.8-x}Sm_xSr_{0.2}Fe_2O_4$ (x = 0.02, 0.04, 0.06, 0.08, 0.1), the nitrates of nickel, strontium, samarium and iron were taken in 20 mL distil water. To this beaker after solubility of all nitrates, citric acid (1:3) portion was added and reaction continued,

stirring maintained at temperature 80 °C. For maintaining the neutral condition, the ammonia solution was added in stoichiometric amount. After continuous heating the solution get converted into gel. Again, gel was completely dried within the next 3 h to afford fine powder. This raw powder was calcinated at 1000 °C for 7 h to get pure ferrite nanomaterial.

2.3 Procedure for Antimicrobial Activity

$Ni_{0.8-x}Sm_xSr_{0.2}Fe_2O_4$ nanoparticles were tested against both Gram-negative and Gram-positive and fungal pathogens using agar well diffusion method [49]. The compounds were added in DMSO to reach final concentration 5 mg/mL. Standard antimicrobial drugs used for bacteria and fungi were streptomycin and clotrimazole respectively. Pathogenic cultures were transferred into sterile nutrient broth and incubated at 37 °C for 24 h. These broths containing pathogens were diluted with sterile saline to reach the turbidly to 0.5 McFarland standards. A 200 μL diluted suspension of pathogen was spread inoculated on Mueller Hinton agar plates separately. Wells were created on sterile agar plates and 100 μL of each compound was added in the well separately. One hundred microlitres of DMSO without compound was also added in separate well as negative control. Plates were incubated at 37 °C for 24 h. Plates were observed for zone of growth inhibition; absence of growth surrounding the well indicates the positive result. The zone of inhibition was recorded in millimetre (mm).

3 Result and Discussion

A series of $Ni_{0.8-x}Sm_xSr_{0.2}Fe_2O_4$ (x = 0.02, 0.04, 0.06, 0.08, 0.1) has been successfully synthesized by employing the sol–gel technique. A UV–visible spectrophotometer is used to determine the absorption peak and band gap of a series. XRD was used to determine particle size, crystal structure, X-ray density, octahedral and tetrahedral sites, and interplanar distance. Field-emission scanning electron microscopy was used to determine structural morphology (FE-SEM). The elemental analysis of a series is provided by energy-dispersive spectroscopy (EDS). Vibrating sample magnetometer was used to investigate the magnetic characteristics (VSM). The average surface area was calculated using BET analysis as well as dielectric and microbial property studies.

3.1 Thermal Analysis

As shown in Fig. 1 the TGA curves from room temperature to 800 °C. At 150 °C the TGA curve was observed due to the weight loss of hydrated water from dried sample. The

second portion of temperature range from 200 to 750 °C was associated with the decomposition of metal hydroxides in their respective metal oxide and loss of NH_3 gas. In addition, the larger weight loss in the second portion of peaks tends to show the response of nitrates and citric acid that eventually formed metal oxides. The endothermic peaks from 300 to 750 °C display the decomposition of unreacted citric acid [50]. For the successive formation of synthesized ferrite in spinel phase, the dried product was calcinated for 7 h at 1000 °C. The material shows 16% loss within 2 steps. So, synthesized material is 84% thermally stable. The thermal analysis was taken for a crude product, and the purpose of the analysis was to check the thermal stability of the material [51, 28, 52].

Fig. 1

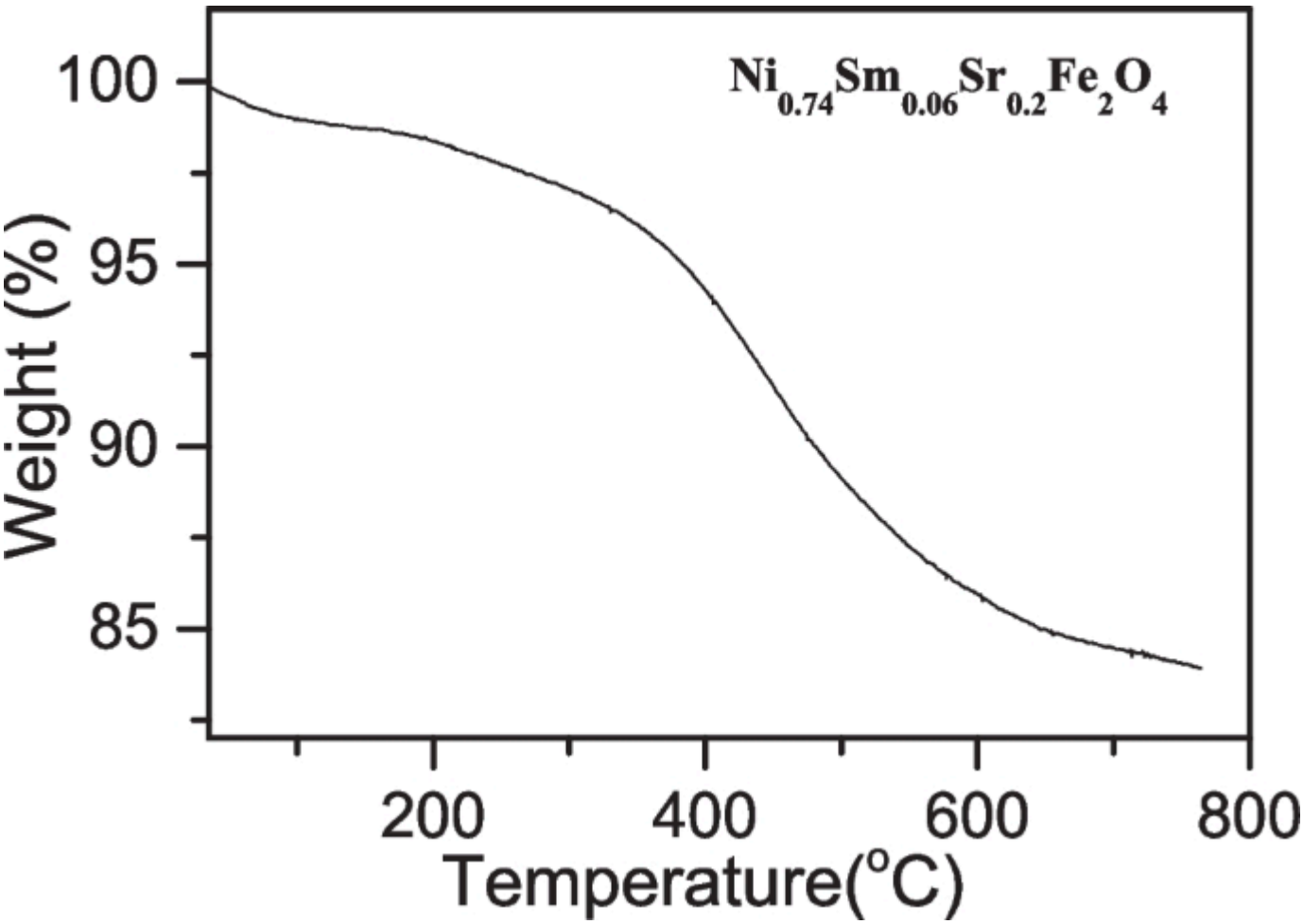

TGA curve of $Ni_{0.8-x}Sm_xSr_{0.2}Fe_2O_4$

3.2 X-ray Analysis

XRD patterns of $Ni_{0.8-x}Sm_xSr_{0.2}Fe_2O_4$ (x = 0.02, 0.04, 0.06, 0.08, 0.1) ferrites, calcined at 1000 °C for 7 h, are shown in Fig. 2. The reflections from (111), (220), (300), (311), (222), (400), (411), (422), (511), and (440) planes confirmed a spinel cubic unit cell, and (311) plane shows the spinel phase structure [34, 35]. So, these allowed planes confirmed the formation of single-phase having a cubic spinel structure. The crystallite size was found in the range from 30 to 60 nm. The inter planar distance (d), lattice parameter (a), volume (V) and X-ray density (d_x), average particle size (D), hopping lengths 'L_A' and 'L_B' and crystal structure of all the composition have been calculated and are reported in Table 1.

Fig. 2

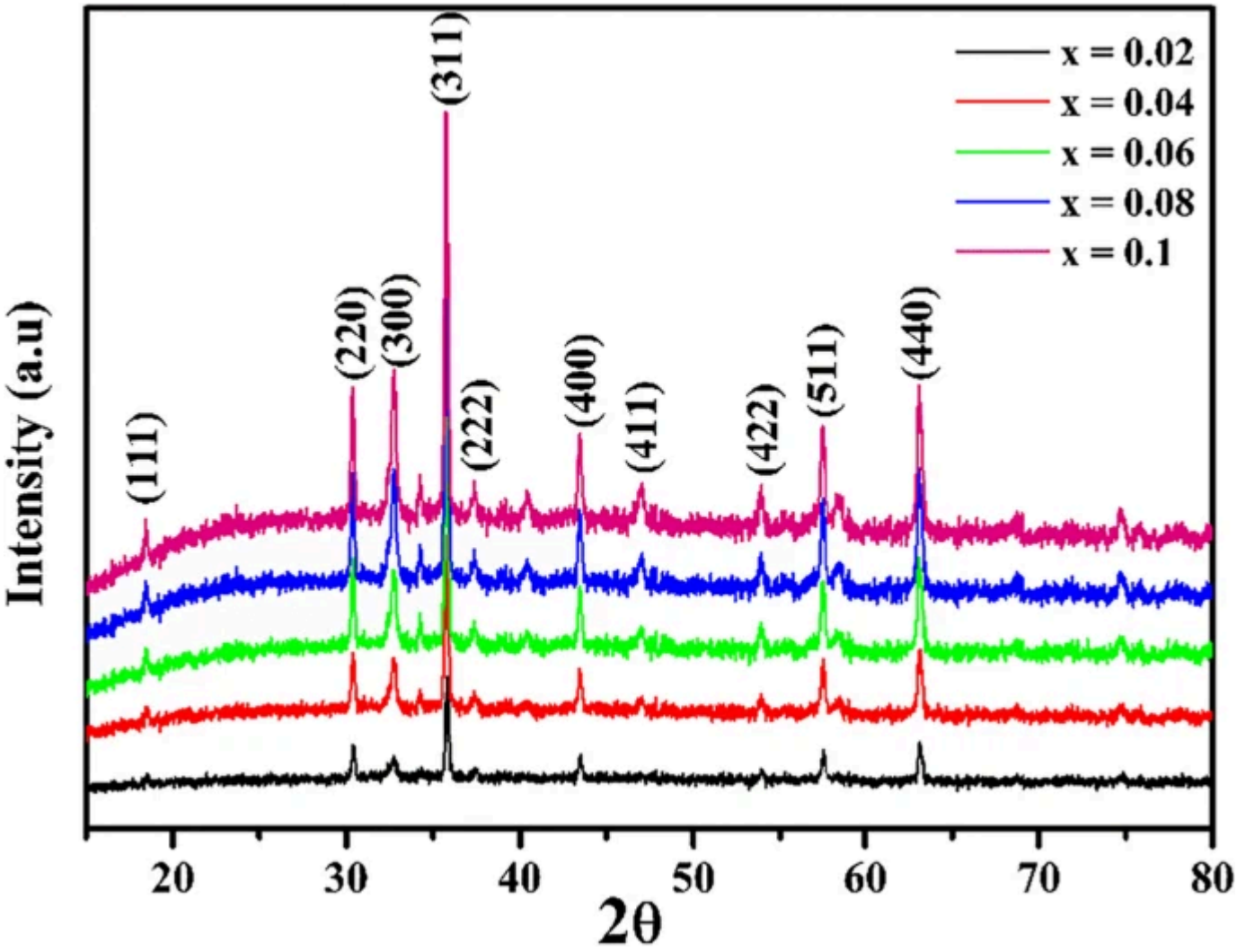

X-ray pattern of $Ni_{0.8-x}Sm_xSr_{0.2}Fe_2O_4$

Table 1 Inter planar distance (d), lattice constant (a), volume (V) and X-ray density (d_x), average particle size (D), hopping lengths 'L_A' and 'L_B' and crystal structure of $Ni_{0.8-x}Sm_xSr_{0.2}Fe_2O_4$

A graph between the lattice parameter and crystalline size with composition is shown in Fig. 3. The crystalline size was calculated by using Debye Scherrer's equation as,

$$\textrm{D}=\frac{0.9\uplambda}{\upbeta\ \textrm{cos}\uptheta}$$

Fig. 3

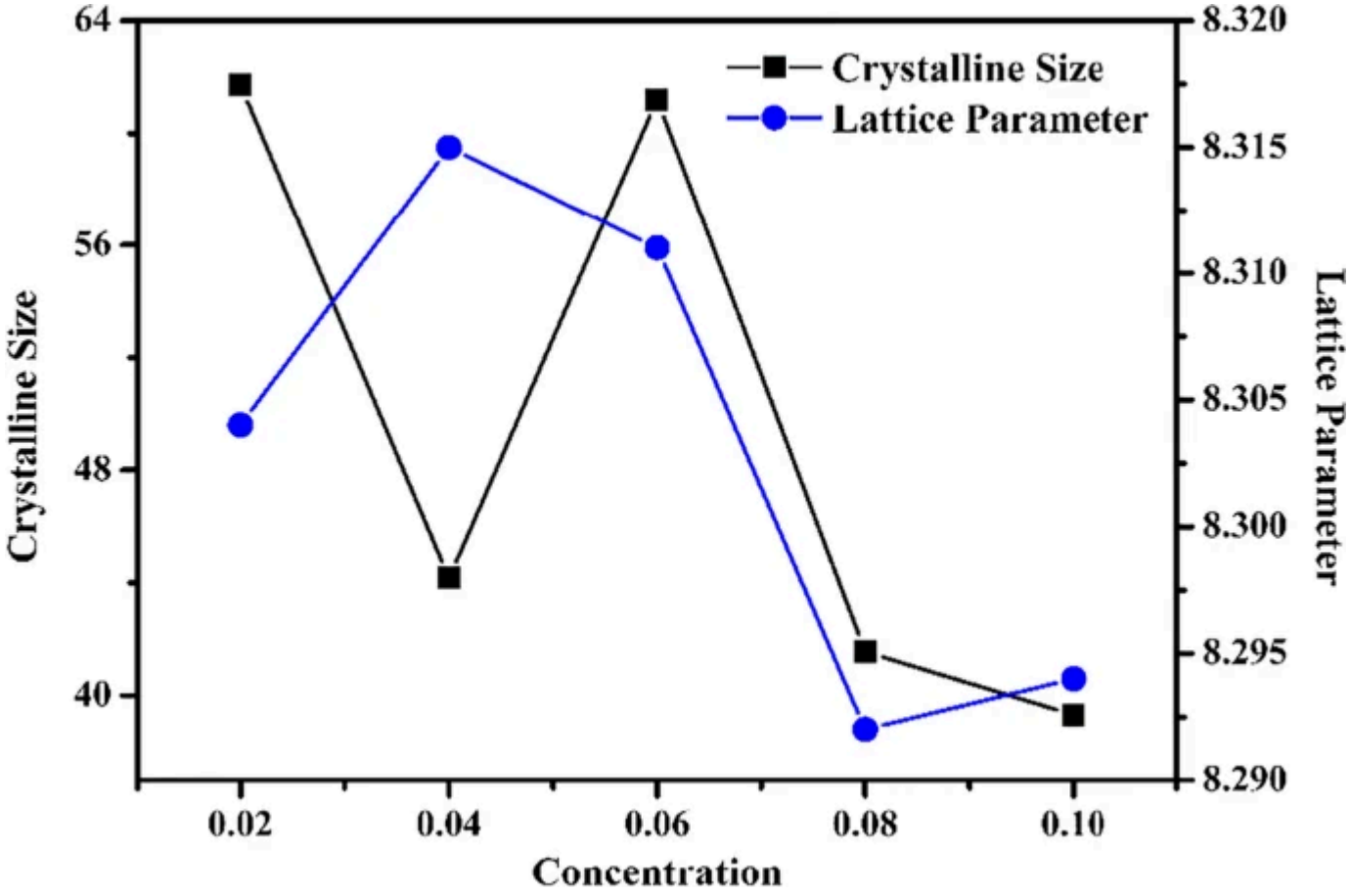

Disparity of crystalline size and lattice parameter of $Ni_{0.8-x}Sm_xSr_{0.2}Fe_2O_4$

It illustrates the variation of lattice constant with Sm^{3+} content in ferrite. This is attributed to the replacement of smaller ionic radii Fe^{3+} by larger ionic radii Sm^{3+} ions.

Figure 4 shows the X-ray density (dx) and unit cell volume (V) with Sm^{3+} concentration. The X-ray density (dx) is depending on the lattice parameter and molecular weight of the sample.

$$\textrm{dx}=\frac{8\textrm{M}}{\textrm{NV}}$$

Fig. 4

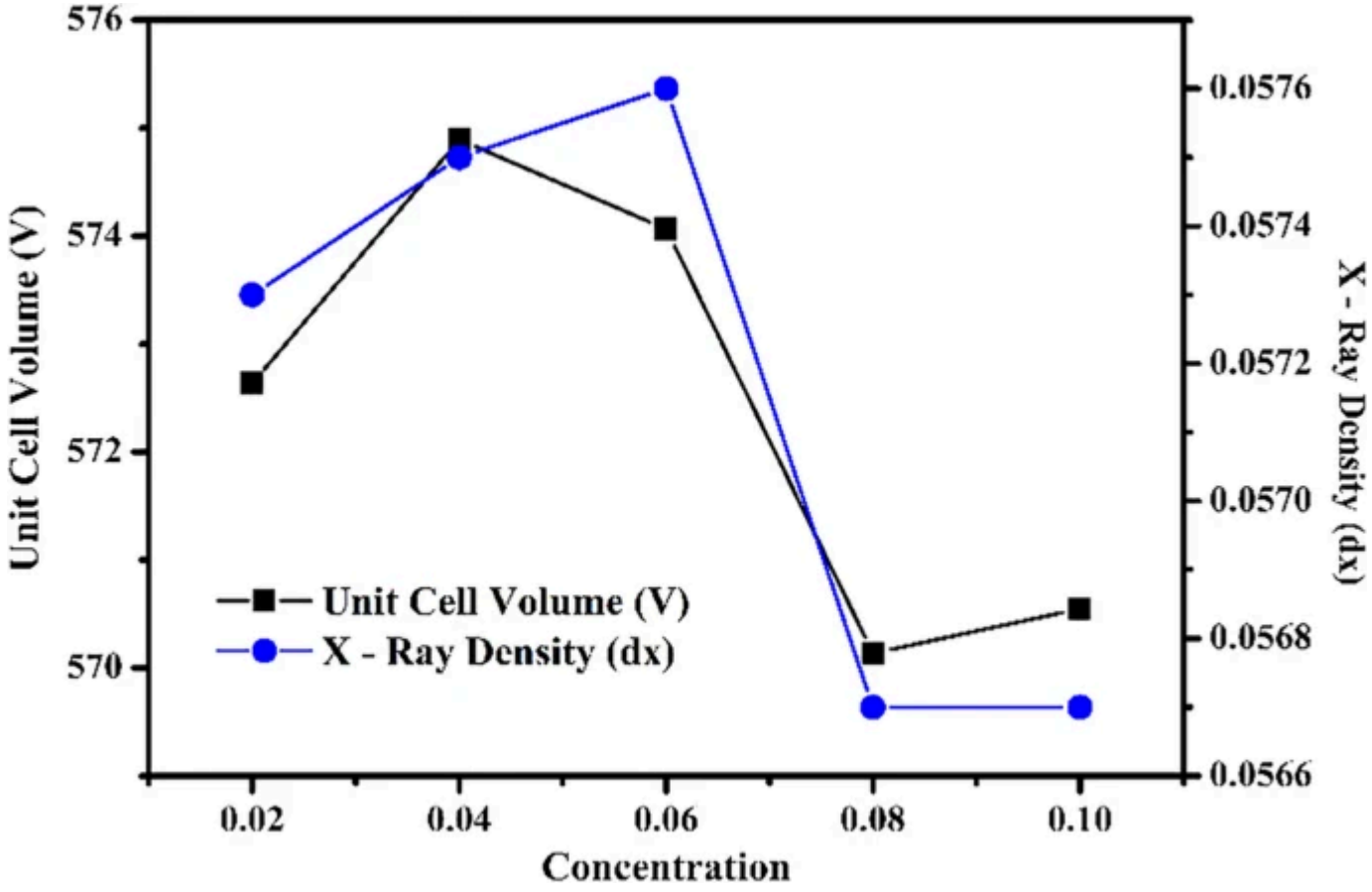

Distinction of unit cell volume and X-ray density of $Ni_{0.8-x}Sm_xSr_{0.2}Fe_2O_4$

Figure 5 depicts the variation in hopping lengths of octahedral and tetrahedral sites with concentration and are calculated by using following formulas,

$$\textrm{LA}=\textrm{a}\frac{\sqrt{3}}{4}\ \textrm{and}\ \textrm{LB}=\textrm{a}\frac{\sqrt{2}}{4}$$

Fig. 5

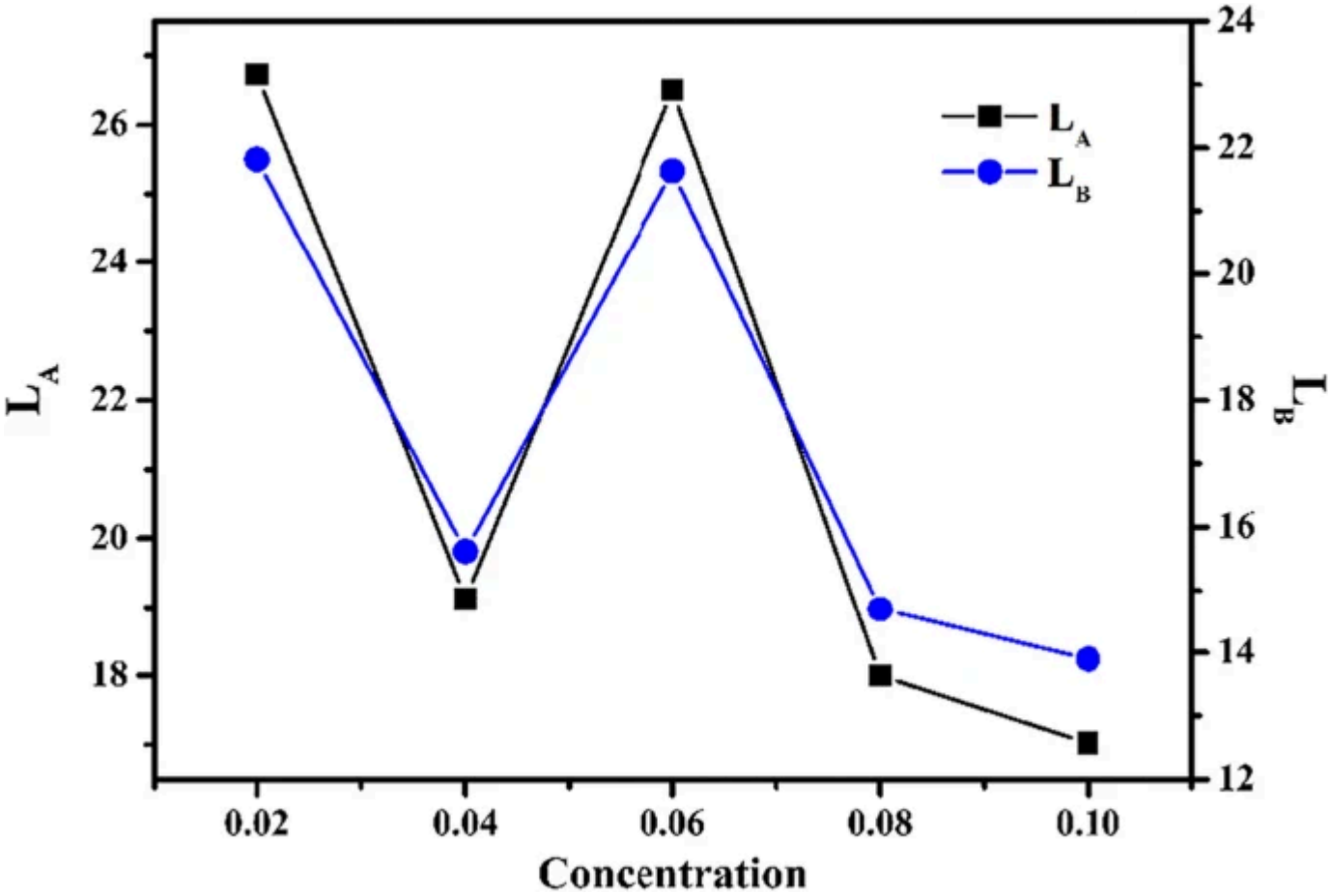

Discrepancy of hopping length of $Ni_{0.8-x}Sm_xSr_{0.2}Fe_2O_4$

3.3 Field-Emission Scanning Electron Microscopy and Energy-Dispersive X-ray Spectroscopy

The microstructure and morphology of prepared samples using a field-emission scanning electron microscope (FE-SEM). The SEM images of $Ni_{0.8-x}Sm_xSr_{0.2}Fe_2O_4$ are shown in Fig. 6 (a–e). The microstructure of the sample varies as the concentration of samarium changes. The concentration of samarium increases with a constant concentration of strontium; the nanoparticles are distributed equally and show the cubic structure. Moreover, it is obvious that the particle size is between 40 and 80 nm [34]. Some agglomerates with an irregular shape were also seen. Therefore, the samples reveal multi-domain behaviour [53,54,55,56].

Fig. 6

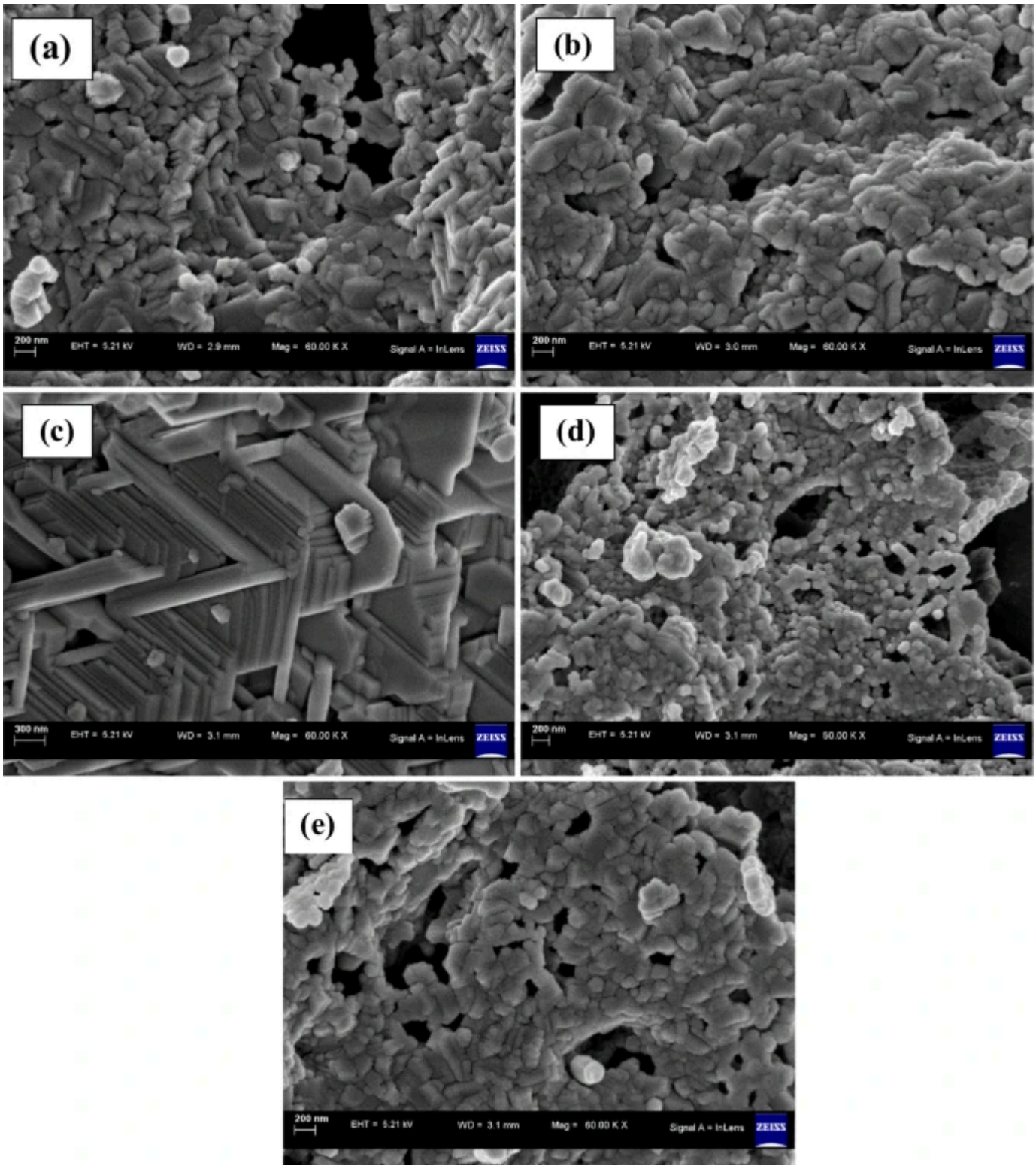

SEM images of $Ni_{0.8-x}Sm_xSr_{0.2}Fe_2O_4$ (200 nm scale bar for each image) for different atomic weight percent (**a**) 0.02, (**b**) 0.04, (**c**) 0.06, (**d**) 0.08, and (**e**) 0.1

Elemental analysis of $Ni_{0.8-x}Sm_xSr_{0.2}Fe_2O_4$ (x = 0.02, 0.04, 0.06, 0.08, and 0.1) was done using the EDS technique shown in Fig. 7 (a–e). All the elements are present, and no extra or impurity peaks are present. The weight percentage and atomic percentage are shown

in Tables 2 and 3, respectively. The weight percentage and atomic percentage are equal to 100% which shows the purity of material.

Fig. 7

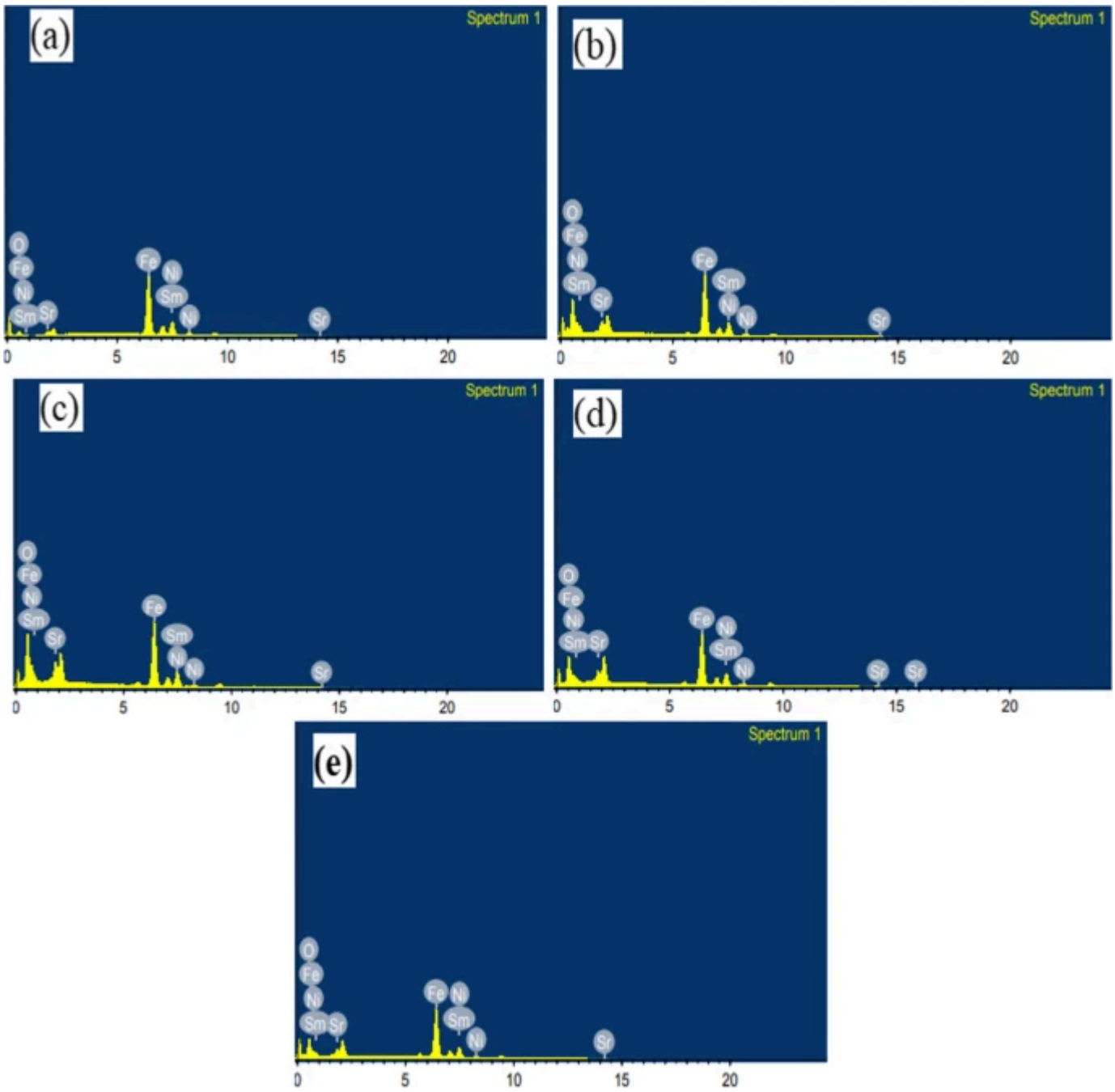

EDS spectrum of $Ni_{0.8-x}Sm_xSr_{0.2}Fe_2O_4$ for different atomic weight percent (**a**) 0.02, (**b**) 0.04, (**c**) 0.06, (**d**) 0.08, and (**e**) 0.1

Table 2 The elements of each sample composition $Ni_{0.8-x}Sm_xSr_{0.2}Fe_2O_4$ nanoparticles

analysed by (weight %) obtained by EDS

Table 3 The elements of each sample composition $Ni_{0.8-x}Sm_xSr_{0.2}Fe_2O_4$ nanoparticles analysed by (Atomic %) obtained by EDS

3.4 Transmission Electron Microscopy

Figure 8 (a–e) displays the TEM images of the synthesized materials. TEM analysis was used to verify the size of the particles. The instigated particle size corresponds with the XRD data. The results indicate that the particles are evenly dispersed, as can be seen in the micrographs. This is caused by the sample's strong magnetic properties. It is revealed that the particle size calculated from TEM data is more accurate than the crystallite size calculated from XRD data. The TEM micrograph at high magnetization shows that most of the particles appear to be cuboidal in shape and are agglomerated to some extent. The average grain size of materials is 40 to 80 nm from SEM morphology, which is in good agreement with TEM.

Fig. 8

TEM of $Ni_{0.8-x}Sm_xSr_{0.2}Fe_2O_4$ for different atomic weight percent (**a**) 0.02, (**b**) 0.04, (**c**) 0.06, (**d**) 0.08, and (**e**) 0.1

3.5 BET Analysis

The surface area and porosity of the resulted nanomaterials were measured using the Brunauer–Emmett–Teller (BET) equation [57]. Figure 9 (a–e) shows the BET surface area from the N_2 adsorption–desorption isotherm of $Ni_{0.8-x}Sm_xSr_{0.2}Fe_2O_4$; the BET surface area of the particles ranges from 13.77 to 28.29 m g^{-1}. The total pore volume at P/Po (0.99) is between 0.02 and 0.04 cm^3g^{-1}. The surface area, pore volume, and pore diameter of all the concentrations are tabulated in Table 4. The average pore diameter was found to be 3.5 to 6.5 nm. The isotherm represents type III, with an H_3 hysteresis loop, which is a characteristic of mesoporous materials. The surface effects are the result of finite-size scaling of crystallites, which in turn leads to a non-collinearity of magnetic moments on their surfaces.

Fig. 9

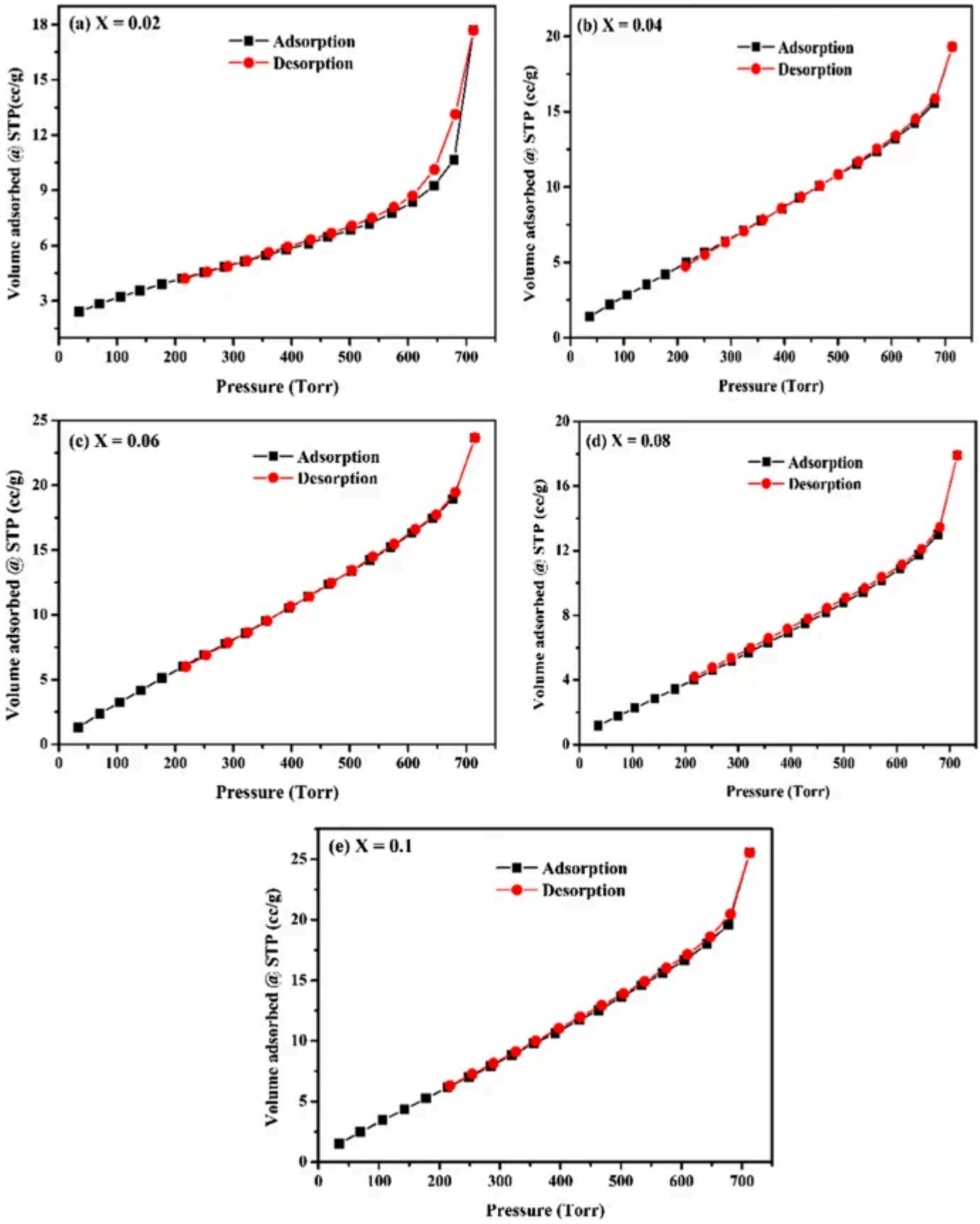

BET adsorption isotherm of $Ni_{0.8-x}Sm_xSr_{0.2}Fe_2O_4$ for different atomic weight percent (**a**) 0.02, (**b**) 0.04, (**c**) 0.06, (**d**) 0.08, and (**e**) 0.1

Table 4 BET data of $Ni_{0.8-x}Sm_xSr_{0.2}Fe_2O_4$

3.6 Vibrating Sample Magnetometer

Figure 10 illustrates the M-H loops taken at room temperature for $Ni_{0.8-x}Sm_xSr_{0.2}Fe_2O_4$ (x = 0.02, 0.04, 0.06, 0.08, 0.1) concentration as a function of the applied magnetic field H. Table 5 shows the saturation magnetization (Ms), remanence magnetization (Mr), coercivity (Hc), squareness ratio, Bohr magnetization, and anisotropy constant (K_1) measured from these loops. The enclosure of Hc implies that these materials are soft magnetic. Spinel ferrites can have three different types of interactions: A-B, A-A, and B-B. The A-B interaction represents the most prevalent of the three [4]. The experimental μ_B per formula unit was calculated as follows:

$${\mu}_B\frac{\textrm{M}\ \textrm{x}}{M}_s}{5585}$$

Fig. 10

Magnetic hysteresis loop of $Ni_{0.8-x}Sm_xSr_{0.2}Fe_2O_4$

Table 5 Magnetization data of $Ni_{0.8-x}Sm_xSr_{0.2}Fe_2O_4$

The consequent elevation in Ms and Mr might be attributed to the significant A-B exchange interactions. The squareness ratio has been seen to increase in value. Prepared samples behave as single-domain particles if the squareness ratio is less than 0.5. Hc coercivity is influenced by various parameters such as magnetic domain size, particle shape, grain size, magneto-crystalline anisotropy, and so on. Larger grains have a higher number of domain barriers. As a result, when these domain walls are magnetic or de-magnetized, domain wall movement consumes less energy than domain rotation [14].

Figure 11 exhibits an increase in saturation magnetization and remanence magnetization as concentration increases. In contrast to domain rotation's contribution to magnetization or demagnetization, wall movement rises as the number of walls increases with grain size. As a result, samples with larger grains should have lower coercivity, and vice versa. This might explain the compositions' progressive increase and reduction in coercivity. Figure 12 shows more the Bohr magnetization and anisotropy constant increase with increasing samarium concentration. Using the relation, the anisotropic constant K_1 is calculated.

$$\textrm{K}1=\frac{M_s{H}_c}{2}\textrm{x}\ 104$$

Fig. 11

Variation of Ms and Mr of $Ni_{0.8-x}Sm_xSr_{0.2}Fe_2O_4$

Fig. 12

Variation of μ_B and K_1 of $Ni_{0.8-x}Sm_xSr_{0.2}Fe_2O_4$

The anisotropy constant also shows properties of coercivity, i.e., gradual decrease and then increase [58], as all exhibiting data of coercivity as well as Bohr magnetization values containing the paramagnetic behaviour.

3.7 UV–Visible Spectroscopy

The UV–visible spectrophotometer is used to analyse the optical characteristics of a $Ni_{0.8-x}Sm_xSr_{0.2}Fe_2O_4$ (x = 0.02, 0.04, 0.06, 0.08, and 0.1). As a consequence of the experiment, all samples could be analysed using the maximum absorption peaks at 302.34 nm. Table 6 displayed that the band gap of all samples ranged from 3.4 to 3.7 eV. The confirming nickel concentration was decreased by doping of the Sm^{3+} ion, which resulted in a band gap increase due to the ionic size of strontium as well as the samarium composition. The UV–visible spectrum and the band gap spectrum are depicted in Fig. 13(a) and (b).

Table 6 Optical band gap of $Ni_{0.8-x}Sm_xSr_{0.2}Fe_2O_4$

Fig. 13

(**a**) UV–visible spectra of $Ni_{0.8-x}Sm_xSr_{0.2}Fe_2O_4$; (**b**) optical band gap of $Ni_{0.8-x}Sm_xSr_{0.2}Fe_2O_4$

3.8 Dielectric Study

To examine the dielectric performance, the dielectric constant (ε') and dielectric loss (ε") of the $Ni_{0.8-x}Sm_xSr_{0.2}Fe_2O_4$ nanoparticles as they were synthesized were studied. The decreasing values of the dielectric constant with increasing frequency are shown in Fig. 14(a). According to the Koop's phenomenological theory, this variation in the dielectric constant highlights the dispersion that was caused by Maxwell interfacial polarization. The hopping of electrons between Ni^{2+} and Fe^{3+} ions may be the source of the dielectric constant's dispersion. $Ni_{0.8-x}Sm_xSr_{0.2}Fe_2O_4$ shows high values of the dielectric constant may be explained by the substitution of nickel and samarium for Fe^{3+}, which was predicted to enhance the density of vacancies and the probability of hopping conduction mechanisms. The Koop's model was supported by the first, gradual decline in dielectric constant. Because of the grains and grain boundaries' high dielectric values, variability developed. Figure 14(b) shows the room temperature frequency evolution of the dielectric loss for $Ni_{0.8-x}Sm_xSr_{0.2}Fe_2O_4$ nanoceramics by using dissipative factor (tan δ). It

demonstrates that as the frequency rises, the dielectric loss drops significantly. Without a loss peak, the dielectric loss rises for all samples with decreasing frequency.

Fig. 14

(**a**) Relationship between dielectric constant and frequency (**b**) Plot of dielectric loss tangent verses frequency

3.9 Antimicrobial Activity

The concentration of compounds 0.04, 0.06, 0.08 and 0.1 showed activity against the *Bacillus Subtilis* ATCC 6633, *Staphylococcus aureus* (ATCC6538), and *Escherichia coli* (ATCC 8739). NPs can interact with lipid content from the cell membrane and lead to pore formation that leads to cell growth inhibition [50]. The antifungal activity was observed with 0.04, 0.06, and 0.1 samples against fungal pathogens. 0.04 compounds were more active against *Aspergillus niger* ATCC 16404, and *Candida albicans* ATCC 10231. Zone of inhibition was not observed with DMSO. Standard drugs streptomycin and clotrimazole showed antimicrobial activity against all pathogens (Table 7) (Graph 1).

Table 7 Antimicrobial activity of $Ni_{0.8-x}Sm_xSr_{0.2}Fe_2O_4$ nanoparticles against microbial pathogens[a]

Graph 1

Antimicrobial activity of nanoparticles against different microbial pathogens

4 Conclusion

The $Ni_{0.8-x}Sm_xSr_{0.2}Fe_2O_4$ nanoparticles were successfully synthesized by using the sol–gel auto combustion method. The material shows 84% thermal stability. The XRD data reveals the cubic spinel structure with particle sizes ranging from 30 to 60 nm. The SEM micrograph shows cubic-shaped granular structure. The elemental analysis shows no extra peaks. So, all elements are present and pure, as well as size and morphology, which are verified by TEM. The BET adsorption isotherm shows total surface area ranging from 13.77 to 28.49 m^2g^{-1}. The total pore volume at P/Po (0.99) is between 0.02 and 0.04 cm^3g^{-1}. The average pore diameter was found to be 3.5 to 6.5 nm. The isotherm represents type III, with an H_3 hysteresis loop. The VSM data shows the synthesized nanoparticles are paramagnetic in nature, with coercivity ranging from 259 to 504 Oe along with Bohr magnetization ranging from 1.95 to 9.63 BM. Their Bohr magneton is enhanced as the anisotropic constant value increases. The band energy range was observed from 3.4 to 3.7 eV at optical density at 302.34 nm. The dielectric loss and dielectric tangent loss show steady loss. These synthesized nanoparticles are showing activity against both Gram-positive and Gram-negative bacterial pathogens *Bacillus*

Subtilis ATCC 6633, *Staphylococcus aureus* (ATCC6538), and *Escherichia coli* (ATCC 8739) as well as against fungal pathogens Aspergillus *niger* ATCC 16404, and *Candida albicans* ATCC 10231.

Data availability

All characterised data are available within the manuscript.

References

1. Mathew, D. S., & Juang, R.-S. (2007). An overview of the structure and magnetism of spinel ferrite nanoparticles and their synthesis in microemulsions. *Chemical Engineering Journal, 129*(1), 51–65. https://doi.org/10.1016/j.cej.2006.11.001

Article Google Scholar

2. Gadkari, A., Shinde, T., & Vasambekar, P. (2010). Influence of rare-earth ions on structural and magnetic properties of $CdFe_2O_4$ ferrites. *Rare Metals, 29*(2), 168–173. https://doi.org/10.1007/s12598-010-0029-z

Article Google Scholar

3. Al-Hilli, M. F., Li, S., & Kassim, K. S. (2012). Structural analysis, magnetic and electrical properties of samarium substituted lithium–nickel mixed ferrites. *Journal of Magnetism and Magnetic Materials, 324*(5), 873–879. https://doi.org/10.1016/j.jmmm.2011.10.005

Article Google Scholar

4. Şabikoğlu, İ., & Parali, L. (2014). FTIR and VSM properties of samarium-doped nickel ferrite. *Functional Materials Letters, 07*. https://doi.org/10.1142/s1793604714500465

5. Bhosale, R. R., Kumar, A., AlMomani, F., Ghosh, U., & Khraisheh, M. (2017). A comparative thermodynamic analysis of samarium and erbium oxide based solar

thermochemical water splitting cycles. *International Journal of Hydrogen Energy, 42*(37), 23416–23426. https://doi.org/10.1016/j.ijhydene.2017.03.172

Article Google Scholar

6. Rashmi, S. K., Bhojya Naik, H. S., Jayadevappa, H., Viswanath, R., Patil, S. B., & Madhukara Naik, M. (2017). Solar light responsive Sm-Zn ferrite nanoparticle as efficient photocatalyst. *Materials Science and Engineering: B, 225*, 86–97. https://doi.org/10.1016/j.mseb.2017.08.012

Article Google Scholar

7. Rashmi, S. K., Naik, H. S. B., Jayadevappa, H., Sudhamani, C. N., Patil, S. B., & Naik, M. M. (2017). Influence of Sm^{3+} ions on structural, optical and solar light driven photocatalytic activity of spinel $MnFe_2O_4$ nanoparticles. *Journal of Solid State Chemistry, 255*, 178–192. https://doi.org/10.1016/j.jssc.2017.08.013

Article Google Scholar

8. Samoila, P., Cojocaru, C., Sacarescu, L., Dorneanu, P. P., Domocos, A.-A., & Rotaru, A. (2017). Remarkable catalytic properties of rare-earth doped nickel ferrites synthesized by sol-gel auto-combustion with maleic acid as fuel for CWPO of dyes. *Applied Catalysis B: Environmental, 202*, 21–32. https://doi.org/10.1016/j.apcatb.2016.09.012

Article Google Scholar

9. Tahir Farid, H. M., Ahmad, I., Bhatti, K. A., Ali, I., Ramay, S. M., & Mahmood, A. (2017). The effect of praseodymium on cobalt-zinc spinel ferrites. *Ceramics International, 43*(9), 7253–7260. https://doi.org/10.1016/j.ceramint.2017.03.016

Article Google Scholar

10. Almessiere, M. A., Slimani, Y., & Baykal, A. (2018). Structural and magnetic properties of Ce-doped strontium hexaferrite. *Ceramics International, 44*(8), 9000–

9008. https://doi.org/10.1016/j.ceramint.2018.02.101

Article Google Scholar

11. Ashraf, G. A., Zhang, L., Abbas, W., & Murtaza, G. (2018). Synthesis and characterizations of Al-Sm substituted Ba-Sr M-type hexagonal ferrite nanoparticles via sol-gel route. *Ceramics International*, 44(15), 18678–18685. https://doi.org/10.1016/j.ceramint.2018.07.096

Article Google Scholar

12. Dahiya, M. S., Tomer, V. K., & Duhan, S. (2018). 31 - Metal–ferrite nanocomposites for targeted drug delivery. In A. A. M. Inamuddin & A. Mohammad (Eds.), *Applications of nanocomposite materials in drug delivery* (pp. 737–760). *Woodhead Publishing*. https://doi.org/10.1016/B978-0-12-813741-3.00032-7

Chapter Google Scholar

13. Slimani, Y., Güngüneş, H., Nawaz, M., Manikandan, A., El Sayed, H. S., Almessiere, M. A., Sözeri, H., Shirsath, S. E., Ercan, I., & Baykal, A. (2018). Magneto-optical and microstructural properties of spinel cubic copper ferrites with Li-Al co-substitution. *Ceramics International*, 44(12), 14242–14250. https://doi.org/10.1016/j.ceramint.2018.05.028

Article Google Scholar

14. Srinivasamurthy, K. M., Angadi, V. J., Kubrin, S. P., Matteppanavar, S., Kumar, P. M., & Rudraswamy, B. (2018). Evidence of enhanced ferromagnetic nature and hyperfine interaction studies of Ce-Sm doped Co-Ni ferrite nanoparticles for microphone applications. *Ceramics International*, 44(15), 18878–18885. https://doi.org/10.1016/j.ceramint.2018.07.123

Article Google Scholar

15. Tiwari, S., & Vitta, S. (2018). Magnetoelectric and magnetodielectric coupling and microwave resonator characteristics of $Ba_{0.5}Sr_{0.5}Nb_2O_6/CoCr_{0.4}Fe_{1.6}O_4$ multiferroic composite. *Scientific Reports, 8*(1), 11619. https://doi.org/10.1038/s41598-018-30132-2

Article Google Scholar

16. Xie, T., Xu, L., Liu, C., Yang, J., Zhang, X., Tian, M., & Cui, C. (2018). Preparation and magnetic properties of Sm–Co doped strontium ferrite. *Materials Technology, 33*(7), 467–473. https://doi.org/10.1080/10667857.2018.1465746

Article Google Scholar

17. Almessiere, M. A., Slimani, Y., Ali, S., Baykal, A., Ercan, I., & Sozeri, H. (2019). Nd^{3+} ion-substituted $Co_{1-2x}Ni_xMn_xFe_{2-y}Nd_yO_4$ nanoparticles: Structural, morphological, and magnetic investigations. *Journal of Inorganic and Organometallic Polymers and Materials, 29*(3), 783–791. https://doi.org/10.1007/s10904-018-1052-z

Article Google Scholar

18. Almessiere, M. A., Slimani, Y., Güner, S., Baykal, A., & Ercan, I. (2019). Effect of dysprosium substitution on magnetic and structural properties of $NiFe_2O_4$ nanoparticles. *Journal of Rare Earths, 37*(8), 871–878. https://doi.org/10.1016/j.jre.2018.10.009

Article Google Scholar

19. Gajula, G. R., Buddiga, L. R., Chidambara Kumar, K. N., & Dasari, M. (2019). Influence of Sm and Nb on the structural, electric, magnetic and magneto-electric properties of $BaTiO_3$-$Li_{0.5}Fe_{2.5}O_4$ composite ceramics grown by the conventional solid state technique. *Journal of Materials Science: Materials in Electronics, 30*(2), 1262–1274. https://doi.org/10.1007/s10854-018-0394-1

Article Google Scholar

20. Martínez-Pérez, J. P., Bolarín-Miró, A. M., Pedro-García, F., Cortés-Escobedo, C. A., Barba-Pingarrón, A., & Sánchez-De Jesús, F. (2019). Magnetic and dielectric characterization of $_x$BiFeO$_3$:(1-x)SrFe$_{12}$O$_{19}$ multiferroic composites. *Journal of Alloys and Compounds, 808*, 151700. https://doi.org/10.1016/j.jallcom.2019.151700

Article Google Scholar

21. Almessiere, M. A., Slimani, Y., Demir Korkmaz, A., Baykal, A., Albetran, H., Saleh, T. A., Sertkol, M., & Ercan, I. (2020). A study on the spectral, microstructural, and magnetic properties of Eu–Nd double-substituted $Ba_{0.5}Sr_{0.5}Fe_{12}O_{19}$ hexaferrites synthesized by an ultrasonic-assisted approach. *Ultrasonics Sonochemistry, 62*, 104847. https://doi.org/10.1016/j.ultsonch.2019.104847

Article Google Scholar

22. Ashraf, G. A., Rasool, R. T., Hassan, M., & Zhang, L. (2020). Enhanced photo Fenton-like activity by effective and stable Al–Sm M-hexaferrite heterogenous catalyst magnetically detachable for methylene blue degradation. *Journal of Alloys and Compounds, 821*, 153410. https://doi.org/10.1016/j.jallcom.2019.153410

Article Google Scholar

23. Esha, I. N., Munny, K. N., Khan, M. N. I., & Maria, K. H. (2020). (1 - x)$BaTi_{0.5}Mn_{0.5}O_3$ + (x)$Ni_{0.6}Zn_{0.4}Fe_{1.85}Sm_{0.15}O_4$ composite multiferroics: Analyzing the customizing effect on conductive and magnetic properties of $BaTi_{0.5}Mn_{0.5}O_3$ by substituting $Ni_{0.6}Zn_{0.4}Fe_{1.85}Sm_{0.15}O_4$ at different concentrations. *AIP Advances, 10*(12), 125026. https://doi.org/10.1063/5.0028086

Article Google Scholar

24. Meng, X., Wang, Y., Zhao, Y., Zhang, T., Yu, N., Chen, X., Miao, M., & Liu, T. (2020). In-situ exsolution of nanoparticles from Ni substituted $Sr_2Fe_{1.5}Mo_{0.5}O_6$ perovskite oxides with different Ni doping contents. *Electrochimica Acta, 348*, 136351. https://doi.org/10.1016/j.electacta.2020.136351

Article Google Scholar

25. Regulska, E., Breczko, J., Basa, A., & Dubis, A. T. (2020). Rare-earth metals-doped nickel aluminate spinels for photocatalytic degradation of organic pollutants. *Catalysts, 10*(9). https://doi.org/10.3390/catal10091003

26. Shezad, M., Liu, X., Feng, S., Kan, X., Shehzad, T. J., Mudassir, A., Wang, W., & Liu, C. (2020). Investigating the co-substitution impact of yttrium–nickel cations on lattice, morphological and magnetic parameters of SrM based ceramics. *Ceramics International, 46*(7), 8918–8927. https://doi.org/10.1016/j.ceramint.2019.12.138

Article Google Scholar

27. Slimani, Y., Unal, B., Almessiere, M. A., Korkmaz, A. D., Shirsath, S. E., Yasin, G., Trukhanov, A. V., & Baykal, A. (2020). Investigation of structural and physical properties of Eu^{3+} ions substituted $Ni_{0.4}Cu_{0.2}Zn_{0.4}Fe_2O_4$ spinel ferrite nanoparticles prepared via sonochemical approach. *Results in Physics, 17*, 103061. https://doi.org/10.1016/j.rinp.2020.103061

Article Google Scholar

28. Yousaf, M., Akhtar, M. N., Wang, B., & Noor, A. (2020). Preparations, optical, structural, conductive and magnetic evaluations of RE's (Pr, Y, Gd, Ho, Yb) doped spinel nanoferrites. *Ceramics International, 46*(4), 4280–4288. https://doi.org/10.1016/j.ceramint.2019.10.149

Article Google Scholar

29. Abdo, M. A., & El-Daly, A. A. (2021). Sm-substituted copper-cobalt ferrite nanoparticles: Preparation and assessment of structural, magnetic and photocatalytic properties for wastewater treatment applications. *Journal of Alloys and Compounds, 883*, 160796. https://doi.org/10.1016/j.jallcom.2021.160796

Article Google Scholar

30. Almessiere, M. A., Slimani, Y., Algarou, N. A., Gondal, M. A., Wudil, Y. S., Younas, M., Auwal, I. A., Baykal, A., Manikandan, A., Zubar, T. I., Kostishin, V. G., Trukhanov, A. V., & Ercan, I. (2021). Electronic, magnetic, and microwave properties of hard/soft nanocomposites based on hexaferrite $SrNi_{0.02}Zr_{0.02}Fe_{11.96}O_{19}$ with variable spinel phase MFe_2O_4 (M = Mn, Co, Cu, and Zn). *Ceramics International, 47*(24), 35209–35223. https://doi.org/10.1016/j.ceramint.2021.09.064

Article Google Scholar

31. Atta, S., Halder, M., & Meikap, A. (2021). Effect of terbium doping on the optical, electrical and magnetic properties of nanocrystalline nickel ferrite. *Journal of Materials Science: Materials in Electronics, 32*. https://doi.org/10.1007/s10854-021-05407-6

32. Gopal Boda, N. B., Rapolu Sridhar, A., Panasa Reddy, D., & Ravinder. (2021). Thermoelectric power, electrical resistivity and magnetic properties of Ni-Sm nanoparticles. *biointerface research in applied. Chemistry, 11*(1), 7835–7846. https://doi.org/10.33263/BRIAC111.78357846

Article Google Scholar

33. Hashim, M., Boda, N., Ahmed, A., Sharma, S. K., Ravinder, D., Sumalatha, E., Ul-Hamid, A., Ismail, M. M., Chaman, M., Shirsath, S. E., Kumar, R., Kumar, S., Meena, S. S., & Nasir, M. (2021). Influence of samarium doping on structural, elastic, magnetic, dielectric, and electrical properties of nanocrystalline cobalt ferrite. *Applied Physics A, 127*(7), 526. https://doi.org/10.1007/s00339-021-04686-4

Article Google Scholar

34. Khan, M., Bisen, S., Shukla, J., Mishra, A., & Sharma, P. (2021). Investigations on the structural and electrical properties of Sm^{3+}-doped nickel ferrite–based ceramics.

Journal of Superconductivity and Novel Magnetism, 34(3), 763–780. https://doi.org/10.1007/s10948-020-05754-1

Article Google Scholar

35. Selvaraj, S., Gandhi, U., Berchmans, L. J., & Mangalanathan, U. (2021). Effect of magnetic ion substitution on the structure and temperature-dependent magnetic properties of strontium hexaferrite. *Materials Technology, 36*(1), 36–45. https://doi.org/10.1080/10667857.2020.1723832

Article Google Scholar

36. Prodan, A. M., Iconaru, S. L., Chifiriuc, C. M., Bleotu, C., Ciobanu, C. S., Motelica-Heino, M., Sizaret, S., & Predoi, D. (2013). Magnetic properties and biological activity evaluation of iron oxide nanoparticles. *Journal of Nanomaterials, 2013*, 1–7.

Google Scholar

37. Barbara Drašler, D. D., Novak, S., Valant, J., Boljte, S., Otrin, L., Rappolt, M., Sartori, B., Iglič, A., Kralj-Iglič, V., Šuštar, V., Makovec, D., Gyergyek, S., Hočevar, M., Godec, M., & Zupanc, J. (2014). Effects of magnetic cobalt ferrite nanoparticles on biological and artificial lipid membranes. *International Journal of Nanomedicine, 9*, 1559–1581. https://doi.org/10.2147/IJN.S57671

Article Google Scholar

38. Pašukonienė, V., Mlynska, A., Steponkienė, S., Poderys, V., Matulionytė, M., Karabanovas, V., Statkutė, U., Purvinienė, R., Kraśko, J. A., Jagminas, A., Kurtinaitienė, M., Strioga, M., & Rotomskis, R. (2014). Accumulation and biological effects of cobalt ferrite nanoparticles in human pancreatic and ovarian cancer cells. *Medicina, 50*(4), 237–244. https://doi.org/10.1016/j.medici.2014.09.009

Article Google Scholar

39. Hanini, A., Massoudi, M. E., Gavard, J., Kacem, K., Ammar, S., & Souilem, O. (2016). Nanotoxicological study of polyol-made cobalt-zinc ferrite nanoparticles in rabbit. *Environmental Toxicology and Pharmacology, 45*, 321–327. https://doi.org/10.1016/j.etap.2016.06.010

Article Google Scholar

40. Montha, W., Maneeprakorn, W., Buatong, N., Tang, I. M., & Pon-On, W. (2016). Synthesis of doxorubicin-PLGA loaded chitosan stabilized (Mn, Zn)Fe_2O_4 nanoparticles: Biological activity and pH-responsive drug release. *Materials Science and Engineering: C, 59*, 235–240. https://doi.org/10.1016/j.msec.2015.09.098

Article Google Scholar

41. Saini, A., Rana, K., Thakur, A., Thakur, P., Mattei, J. L., & Queffelec, P. (2016). Low loss composite nano ferrite with matching permittivity and permeability in UHF band. *Materials Research Bulletin, 76*, 94–99. https://doi.org/10.1016/j.materresbull.2015.12.002

Article Google Scholar

42. Gomes, G. A., Costa, G. L., & Figueiredo, A. B.-H. S. (2018). Synthesis of ferrite nanoparticles $Cu_{1-x}Ag_xFe_2O_4$ and evaluation of potential antibacterial activity. *Journal of Materials Research and Technology, 7*(3), 381–386. https://doi.org/10.1016/j.jmrt.2018.04.021

Article Google Scholar

43. García-Cruz, A., Rincón-Enríquez, G., Ilyina, A., Guízar-González, C., Mtz-Enríquez, A. I., Díaz-Jiménez, L., Quiñones-Aguilar, E. E., Enríquez-Vara, J., Ramos-González, R., & Aguilar-González, C. N. (2019). Bactericidal in-vitro effect of zinc ferrite nanoparticles and the orange wax extracts on three phytopathogen microorganisms. *IEEE Transactions on NanoBioscience, 18*(4), 528–534. https://doi.org/10.1109/tnb.2019.2937840

Article Google Scholar

44. Thakur, A., Sharma, N., Bhatti, M., Sharma, M., Trukhanov, A. V., Trukhanov, S. V., Panina, L. V., Astapovich, K. A., & Thakur, P. (2020). Synthesis of barium ferrite nanoparticles using rhizome extract of Acorus Calamus: Characterization and its efficacy against different plant phytopathogenic fungi. *Nano-Structures & Nano-Objects, 24*, 100599. https://doi.org/10.1016/j.nanoso.2020.100599

Article Google Scholar

45. Rafiq, S., Aadil, M., Warsi, M. F., Yousaf, S., Alotaibi, M. T., El-Bahy, S. M., & Shahid, M. (2022). NiO nanoparticles and their nanohybrid with flat rGO sheets: As an ideal electroactive material for hybrid capacitor applications. *Ceramics International, 48*(10), 14596–14605. https://doi.org/10.1016/j.ceramint.2022.01.353

Article Google Scholar

46. Rafiq, S., Alanazi, A. K., Bashir, S., Elnaggar, A. Y., Mersal, G. A. M., Ibrahim, M. M., Yousaf, S., & Chaudhary, K. (2022). Optimization studies for nickel oxide/tin oxide (NiO/Xg SnO_2, X: 0.5, 1) based heterostructured composites to design high-performance supercapacitor electrode. *Physica B: Condensed Matter, 638*, 413931. https://doi.org/10.1016/j.physb.2022.413931

Article Google Scholar

47. Yousaf, S., Zulfiqar, S., Somaily, H. H., Warsi, M. F., Rasheed, A., Shahid, M., & Ahmad, I. (2022). An efficient and stable iodine-doped nickel hydroxide electrocatalyst for water oxidation: Synthesis, electrochemical performance, and stability. *RSC Advances, 12*(36), 23454–23465. https://doi.org/10.1039/d2ra03873k

Article Google Scholar

48. Ahmed, S., Ashraf, M., Yousaf, S., Alsafari, I. A., Akhtar, M., Shahid, M., Somaily, H. H., & Warsi, M. F. (2023). High-performance, non-enzymatic glucose sensor based

on Fe and Cu doped ZnO/rGO based nanocomposite. *Materials Chemistry and Physics, 297*, 127335. https://doi.org/10.1016/j.matchemphys.2023.127335

Article Google Scholar

49. Mustafa, A., Alsafari, I. A., Somaily, H. H., Yousaf, S., Din, M. I., Rahman, J., Shahid, M., Ashraf, M., & Warsi, M. F. (2023). Fabrication, characterization of NiO–Co_3O_4/rGO based nanohybrid and application in the development of non-enzymatic glucose sensor. *Physica B: Condensed Matter, 648*, 414404. https://doi.org/10.1016/j.physb.2022.414404

Article Google Scholar

50. Jarvin, M., Kumar, S. A., Vinodhkumar, G., Manikandan, E., & Inbanathan, S. S. R. (2021). Enhanced photocatalytic performance of Hausmannite Mn_3O_4-rGO nanocomposite in degrading methylene blue. *Materials Letters, 305*, 130750. https://doi.org/10.1016/j.matlet.2021.130750

Article Google Scholar

51. Warsi, M. F., Iftikhar, A., Yousuf, M. A., Sarwar, M. I., Yousaf, S., Haider, S., Aly Aboud, M. F., Shakir, I., & Zulfiqar, S. (2020). Erbium substituted nickel–cobalt spinel ferrite nanoparticles: Tailoring the structural, magnetic and electrical parameters. *Ceramics International, 46*(15), 24194–24203. https://doi.org/10.1016/j.ceramint.2020.06.199

Article Google Scholar

52. Yousaf, S., Aadil, M., Zulfiqar, S., Warsi, M. F., Agboola, P. O., Aly Aboud, M. F., & Shakir, I. (2020). Hierarchically porous CuO microspheres and their r-GO based nanohybrids for electrochemical supercapacitors applications. *Journal of Materials Research and Technology, 9*(6), 14158–14167. https://doi.org/10.1016/j.jmrt.2020.09.110

Article Google Scholar

53. Iftikhar, A., Yousaf, S., Ahmed Ali, F. A., Haider, S., Ud-Din Khan, S., Shakir, I., Iqbal, F., & Warsi, M. F. (2020). Erbium-substituted $Ni_{0.4}Co_{0.6}Fe_2O_4$ ferrite nanoparticles and their hybrids with reduced graphene oxide as magnetically separable powder photocatalyst. *Ceramics International, 46*(1), 1203–1210. https://doi.org/10.1016/j.ceramint.2019.08.176

Article Google Scholar

54. Yousaf, S., Zulfiqar, S., Shahi, M. N., Warsi, M. F., Al-Khalli, N. F., Aly Aboud, M. F., & Shakir, I. (2020). Tuning the structural, optical and electrical properties of NiO nanoparticles prepared by wet chemical route. *Ceramics International, 46*(3), 3750–3758. https://doi.org/10.1016/j.ceramint.2019.10.097

Article Google Scholar

55. Yousaf, S., Zulfiqar, S., Shahid, M., Jamil, A., Shakir, I., Agboola, P. O., & Warsi, M. F. (2020). Electrochemical energy storage properties studies of $Cu_{0.2}Ni_{0.8}O$-Reduced graphene oxide nano-hybrids. *Ceramics International, 46*(9), 14304–14310. https://doi.org/10.1016/j.ceramint.2020.02.115

Article Google Scholar

56. Yousaf, S., Zulfiqar, S., Din, M. I., Agboola, P. O., Aly Aboud, M. F., Warsi, M. F., & Shakir, I. (2021). Solar light irradiated photocatalytic activity of ZnO–NiO/rGO nanocatalyst. *Journal of Materials Research and Technology, 12*, 999–1009. https://doi.org/10.1016/j.jmrt.2021.03.012

Article Google Scholar

57. Hussain, N., Alwan, S., Alshamsi, H., & Sahib, I. (2020). Green synthesis of S- and N-codoped carbon nanospheres and application as adsorbent of Pb (II) from aqueous

solution. *International Journal of Chemical Engineering, 2020*, 9068358. https://doi.org/10.1155/2020/9068358

Article Google Scholar

58. Ain, N.-u., Shaheen, W., Bashir, B., Abdelsalam, N. M., Warsi, M. F., Khan, M. A., & Shahid, M. (2016). Electrical, magnetic and photoelectrochemical activity of rGO/$MgFe_2O_4$ nanocomposites under visible light irradiation. *Ceramics International, 42*(10), 12401–12408. https://doi.org/10.1016/j.ceramint.2016.04.179

Article Google Scholar

Acknowledgements

We are thankful to Dr. Babasaheb Ambedkar Marathwada University, Sub-Campus Osmanabad, for performing this study.

Funding

The Chhatrapati Shahu Maharaj Research, Training, and Human Development Institute, Pune, for providing financial support to R. M. Bhore under the SARTHI Fellowship (CSMNRF-2020/2021-22/109).

Author information

Authors and Affiliations

Department of Chemistry, Dr. Babasaheb Ambedkar Marathwada University, Sub campus Osmanabad, Aurangabad, Maharashtra, 413 501, India
Rajkanya M. Bhore, Radhakrishnan M. Tigote, Subiya K. Kazi & Sanjay R. Chavan

Department of Microbiology, Dr. Babasaheb Ambedkar Marathwada University, Sub campus Osmanabad, Aurangabad, Maharashtra, 413 501, India
Rahul M. Khobragade

J.M. Patel Arts, Commerce and Science College, Research Centre, Dr. Babasaheb Ambedkar Marathwada University, Sub campus Osmanabad, Aurangabad, Maharashtra, 413501, India
Girdharilal B. Tiwari

Contributions

Miss. Rajkanya M. Bhore: experimental table work

Dr. Radhakrishnan M. Tigote* (corresponding author): design the new research work and draught the original manuscript

Miss. Subiya K. Kazi: formal analysis

Mr. Sanjay R. Chavan: validation

Dr. Rahul M. Khobragade: study of antimicrobials

Dr. Girdharilal B. Tiwari: methodology

All co-authors have seen and agreed with the contents of the manuscript.

Corresponding author

Correspondence to Radhakrishnan M. Tigote.

Ethics declarations

Consent for Publication

All authors have consented to publish.

Conflict of Interest

The authors declare no competing interests.

Additional information

Publisher's Note

Springer Nature remains neutral with regard to jurisdictional claims in published maps and institutional affiliations.

Rights and permissions

About this article

Cite this article

Bhore, R.M., Tigote, R.M., Kazi, S.K. *et al.* Investigation of Structural and Microbial Properties of Samarium-Doped Nickel-Strontium Ferrite Nanoparticles Prepared via the Sol-Gel Route. *BioNanoSci.* **13**, 1126–1139 (2023). https://doi.org/10.1007/s12668-023-01122-0

Accepted	Published	Issue Date
28 April 2023	19 June 2023	September 2023

DOI
https://doi.org/10.1007/s12668-023-01122-0

Share this article

Keywords

Optical band gap **Magnetic hysteresis** **Dielectric loss**

Microbial activity